Retention or repulsion forces induced by bubbles trapped at the base of an immersed microparticle on a substrate

Anna Ipatova and Alexis Duchesne
Université de Lille, CNRS, ECLille, ISEN, Université Valenciennes, UMR 8520-IEMN, F-59000 Lille, France

H. N. Yoshikawa[*]
Université Côte d'Azur, CNRS, Institut de Physique de Nice, 06100 Nice, France

Pascal Mariot and Corenthin Leroy
Université de Lille, INSERM U1003, Bâtiment SN3, F-59655 Villeneuve d'Ascq, France

Christine Faille
Université de Lille, CNRS, INRAE, ENSCL, UMET, F-59650 Villeneuve d'Ascq, France

Ichiro Ueno
*Department of Mechanical Engineering, Faculty of Science and Technology,
Tokyo University of Science, Chiba 278-8510, Japan*

Georg F. Dietze
Université Paris-Saclay, CNRS, FAST, 91405 Orsay, France

Farzam Zoueshtiagh[†]
*Université de Lille, CNRS, ECLille, ISEN, Université Valenciennes,
UMR 8520-IEMN, F-59000 Lille, France*

We explore the potential for air bubble entrapment beneath micrometer-sized particles following immersion. This investigation employs theoretical, numerical, and experimental methodologies, with a focus on the wetting characteristics of both the particle and its substrate. These properties are crucial in determining the likelihood of entrapment and its impact on the particle's adhesion force to the substrate. The theoretical model provides the mathematical framework to account for the additional force exerted on the particle due to the entrapped bubble, while numerical calculations yield corresponding force values. The results underscore the significant influence of the wettability of both the particle and the substrate on this force. In support of findings of the numerical model, companion experiments were performed. The results demonstrate that the bubbles can indeed be entrapped at microscales underneath micrometric particles. Experimental measurements of detachment force reveal the substantial impact of these entrapped bubbles on the force required to detach particles from a surface. Specifically, the force appears notably higher when either the particle or the substrate, or both, exhibit hydrophobic characteristics. We highlight the alignment observed between numerical calculations and experimental

---

[*]Present address: Faculty of Science and Engineering, Doshisha University, 1-3 Tatara Miyakodani, Kyotanabe-shi, Kyoto, 610-0321 Japan.
[†]Contact author: farzam.zoueshtiagh@univ-lille.fr

results, while also examining and discussing any identified disparities and their root causes. Lastly, we propose an energy model that predicts the post-detachment configuration of the bubble, determining whether it remains attached to the particle, adheres to the substrate, or splits into daughter bubbles distributed across both surfaces. These findings hold significance for a wide range of industrial applications where the immersion of micrometer-sized entities, such as dirt or bacteria, is common during liquid-based cleaning processes.

I. INTRODUCTION

Removing micrometer-sized particles with the lowest energy and water consumption is a major challenge that begs technological solutions in various domains from microtechnology [1–4], automotive [5,6], to food [7–10] industries. This has attracted great attention from the scientific community who investigated various self-cleaning surface solutions using either the hydrophobic or the hydrophilic characteristics of the substrates [11] with usually bioinspired solutions [12–14]. For instance, the self-cleaning ability of lotus leaves on which a liquid drop easily rolls while soaking dirt, has been extensively studied and their superhydrophobic hierarchical surface has been replicated by various techniques [12]. Nevertheless, the various technical solutions proposed are essentially tailored for particles that do not adhere to the substrate initially. Indeed, the interaction between dirt/particle and the substrate can substantially decrease or, at worst, fully suppress the self-cleaning characteristic.

For small particles of less than 50 μm in diameter, the substrate-particle interactions are mainly due to electrostatic and van der Waals molecular interactions [15,16]. Other mechanisms also exist and can have an impact in specific configurations like liquid bridges [16] or chemical bonds [16]. One mechanism that has attracted less attention from the scientific community is the eventual presence of a gas bubble trapped between the particle and the substrate. This situation may well occur at the substrate-liquid immersion throughout, for instance, a classical cleaning procedure. Here we show how a bubble can greatly modify the attachment force of a particle to the substrate depending on their associated wetting characteristics.

To investigate the problem associated with such situation, we developed a theoretical model, ran numerical calculations, and carried out experiments. The model is based on considerations of involved forces in static situations. Supplemented by its companion numerical calculations, it provides us with estimates of the force that a bubble may apply to the particle. In particular, through the numerical modeling, we may conclude the positive and negative role that a bubble can have on holding a particle on a substrate. Thereafter, experimental measurements of the detachment force using the patch-clamp technique are carried out. The data demonstrate the presence of trapped bubbles underneath particles with respect to surface wetting properties. The experimental and numerical data are compared to discuss agreements and differences. A second model based on energy considerations is then advanced with the aim to give insights about how a particle-bubble system is detached from the substrate. Conclusions are finally drawn on the configurations where the bubble can favor the detachment of a particle from a substrate and, therefore, on surface cleaning as a potential application.

II. MODEL

As mentioned before, the adhesion force is a combination of several different mechanisms. However, for simplicity, the current model solely accounts for adhesion resulting from the presence of an air bubble, without incorporating any other forces in the system. Although this may not reflect the whole reality, it provides insights into the contributing role of a trapped bubble in either retaining or repulsing a particle from a substrate.
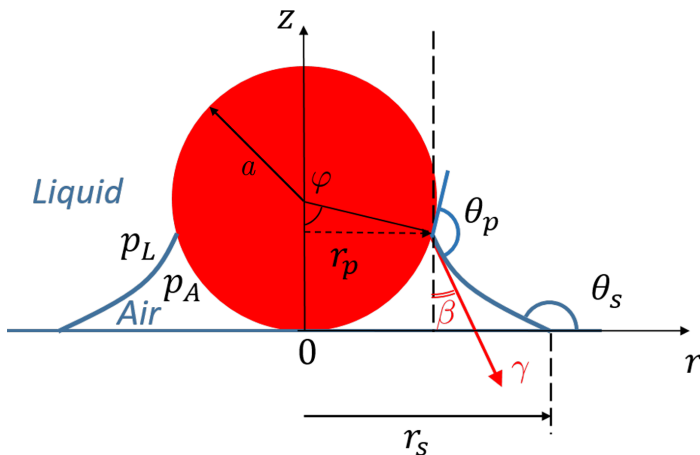
FIG. 1. Air bubble trapped underneath a particle of radius a with the filling angle φ and contact angles θ_p and θ_s.

Here, only micrometric particles of a radius of $a \lesssim 10\,\mu$m are considered. The Bond number, Bo $= \rho g a^2 / \gamma$, comparing the gravity to capillary effects remains small (Bo $\lesssim 10^{-4}$ for typical values of liquid density $\rho \sim 10^3$ kg/m^3 and surface tension $\gamma \sim 10^{-1}$ N/m), and, therefore, the gravity is neglected. The liquid and air pressure, p_L and p_A, are thus supposed to be uniform. Below, we first present the equations modeling a bubble trapped between a particle and a substrate. Then, numerical calculations based on these equations are carried out to compute the force due to capillarity.

A. Forces acting on the particle

We consider a spherical particle of a radius a immersed in a liquid at rest and being in contact with a solid wall (Fig. 1). We introduce the r coordinate along the solid wall, and the central axis z perpendicular to the wall. We assume an axisymmetric system, i.e., the shape of the bubble is invariant against any rotation around the particle central axis z. An air bubble is plugged between the particle and the wall with a given distance r_s of the contact line from the symmetry axis (Fig. 1). The surfaces of the particle and the wall are smooth and their wettabilities are characterized by the static contact angles θ_p and θ_s, respectively. We further neglect any wetting hysteresis effects on either surface.

The angle formed between the z axis and the radius of a particle drawn from its center to the contact line (in studies of liquid bridges under a particle [17,18], this angle is the so-called "filling angle") is denoted by φ. The radius r_p represents the distance of the contact line from the symmetry axis: $r_p = a \sin \varphi$. For brevity, we introduce the symbol β to denote the angle of the particle-liquid-bubble interface measured from the symmetry axis: $\beta = \pi/2 - (\theta_p - \varphi)$.

Considering only capillarity-generated forces, the z component of the force acting on a particle at the particle-bubble interface is given by

$$F_p = F_{p,l} + F_{p,c} = -\pi r_p^2 \Delta p - 2\pi r_p \gamma \, \cos \beta$$
$$= -\pi a^2 \sin^2 \varphi \Delta p - 2\pi a \gamma \, \sin \varphi \, \sin(\theta_p - \varphi), \tag{1}$$

where $F_{p,l}$ is the Laplace pressure force, $F_{p,c}$ is the tensile force acting on the particle contact line at $r = r_p$, and $\Delta p = p_L - p_A$ is the pressure difference.

We compute F_p for given contact angles (θ_p, θ_s) and a given bubble foot radius r_s. The contact angle position φ, involved in Eq. (1) as well as the pressure difference Δp are determined from the

shape of the bubble governed by the Young-Laplace equation:

$$\Delta p = -\gamma (\nabla \cdot \vec{n}), \tag{2}$$

where $\vec{n}$ is the unit normal vector to the interface and is derived from the air-liquid interface shape $r = f(z)$ as

$$\vec{n} = \frac{\vec{e}_r - f_z \vec{e}_z}{\left(1 + f_z^2\right)^{1/2}}, \tag{3}$$

where $f_z = df/dz$. Substituting (3) into Young-Laplace equation (2), one obtains the equation determining the shape of the air-liquid interface

$$\frac{f_{zz}}{\left(1 + f_z^2\right)^{3/2}} - \frac{1}{f\left(1 + f_z^2\right)^{1/2}} = \frac{\Delta p}{\gamma}. \tag{4}$$

This equation is to be solved with varying Δp so that all the following boundary conditions are satisfied:

$$f = r_s, \quad f_z = \cot\theta_s, \quad \text{at } z = 0, \tag{5}$$

$$f_z = -\cot(\theta_p - \varphi), \quad \text{at } z = a(1 - \cos\varphi). \tag{6}$$

The air pressure p_A is computed as

$$p_A = p_L - \Delta p, \tag{7}$$

where Δp is obtained by integrating Eq. (4) using boundary conditions (5) and (6). The pressure p_L is set at 1×10^5 Pa, assuming a pressure in the liquid close to that of the atmosphere.

B. Numerical solution

The geometry of the system, set by the parameters $(\theta_p, \theta_s, r_s)$, allows the determination of $(\Delta p, \varphi)$ through the integration of Eq. (4) with respect to boundary conditions (5) and (6). The force F_p [Eq. (1)] is, then, computed and its positive or negative contribution on holding a particle on the substrate is deduced. The numerical scheme of the integration is given in Appendix A.

In the following, we investigate the effect of various wetting properties for the particle and the substrate on F_p. The results will then enable us to cast the positive or negative role of F_p, hence the bubble, in pushing or holding the particle on the substrate, respectively. The variation of wetting properties is done by varying θ_s for a fixed value of θ_p. In the coming paragraphs, we will first study the case of a hydrophobic and then hydrophilic particle. Hydrophobic and hydrophilic characteristics are accounted for the particle by setting θ_p values to $125°$ and $50°$, respectively. The value of $\theta_p = 125°$ matches the wetting property of the particles tested experimentally as detailed below. Regarding the hydrophilic property represented by the $\theta_p = 50°$ value, it is arbitrarily chosen but in such a way to reduce the numerical difficulties as low θ_p values could not provide mathematical solutions satisfying the boundary conditions. All the numerical simulations are performed for a particle of a radius of $a = 1$ μm surrounded by water ($\gamma = 0.073$ N/m).

Hydrophobic particle ($\theta_p = 125°$). Figure 2 illustrates the shape of the air-liquid interface in three different cases of wetting degree of the substrate characterized by contact angles $\theta_s = 100°$ (blue line), $\theta_s = 50°$ (pink line), and $\theta_s = 10°$ (black line). In these examples, the position of the contact line on the substrate is fixed here at $r_s/a = 0.5$. One can see that the interface shape changes dramatically depending on the substrate wettability θ_s. For a given r_s, it is obvious that the bubble volume is decreasing with the growth of θ_s. The pressure difference Δp reflects the wettability of the substrate: for both hydrophilic substrates, it is $\Delta p \approx -6 \times 10^5$ Pa, while for the hydrophobic substrate $\Delta p \approx -2 \times 10^5$ Pa, which is three times less in magnitude.

For fixed $\theta_p = 125°$, we vary both θ_s and r_s to study their effect on F_p. The contact angles range from hydrophilic $\theta_s = 2°$ to hydrophobic $\theta_s = 140°$. The position of the contact line on the
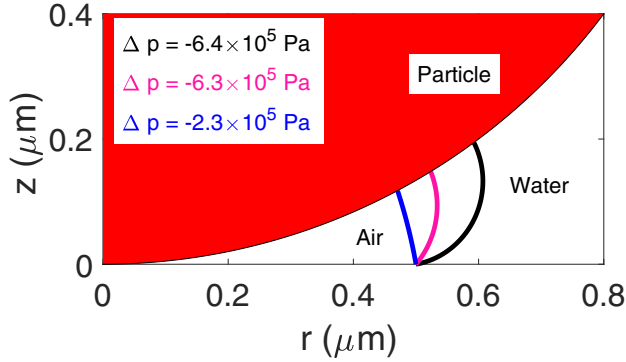
FIG. 2. Shape of the air-liquid interface between a hydrophobic particle ($\theta_p = 125°$) and a hydrophobic substrate with $\theta_s = 100°$ (blue line), and a hydrophilic substrate with $\theta_s = 50°$ (pink line) or $\theta_s = 10°$ (black line). For all these interfaces, $r_s/a = 0.5$.

substrate r_s is varied from $r_s = 0.05$ μm to $r_s = 1$ μm. Figure 3 shows the map of variation of F_p as a function of r_s and θ_s. The red on the map means that the force induced by the bubble is directed up, i.e., would facilitate the detachment from the substrate, while blue is used for the force directed down, that would oppose the particle detachment. The gray color indicates the zone where the air pressure p_A calculated via Eq. (7) is found negative, i.e., no bubble may physically exist or be sustained. The black lines indicate isoforces with their magnitudes (in nanonewtons) displayed on the corresponding line.

The map shows that the contribution of a bubble to the particle detachment clearly depends on the substrate contact angle θ_s and the position of the contact line on the substrate r_s. The force F_p is
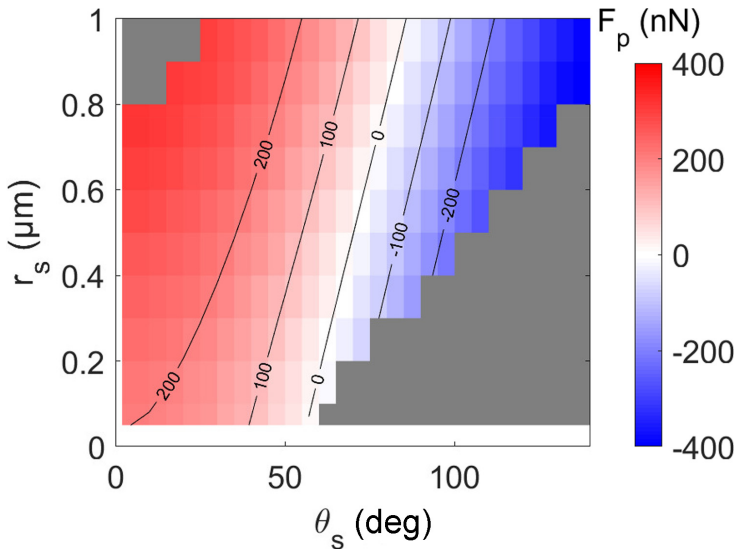
FIG. 3. Map of the force F_p on a hydrophobic particle of radius 1 μm and a contact angle $\theta_p = 125°$ in the r_s-θ_s plane, where r_s is the bubble foot radius and θ_s is the contact angle of the substrate. Red indicates an upward directed force, i.e., facilitating the particle detachment from the substrate, while blue represents the force directed downward. Gray indicates the zone where the pressure in the bubble is found negative and has no physical reality.

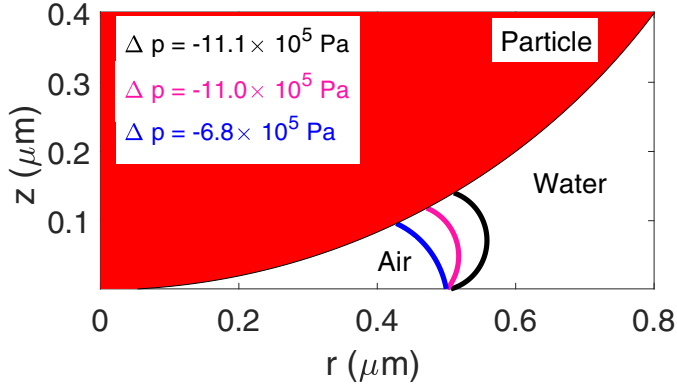FIG. 4. Shape of the air-liquid interface between a hydrophilic particle ($\theta_p = 50°$) and a hydrophobic substrate with $\theta_s = 100°$ (blue line), and a hydrophilic substrate with $\theta_s = 50°$ (pink line) or $\theta_s = 10°$ (black line). For all these interfaces, $r_s/a = 0.5$.

directed upward for hydrophilic substrates with contact angles up to $\theta_s \sim 55°$ regardless of r_s. For $55° \lesssim \theta_s \lesssim 85°$, the positive or negative contribution of F_p depends on r_s; in other words in the size of the bubble. For hydrophobic substrates with contact angles greater or equal to $\theta_s \gtrsim 85°$, the force F_p is directed down for any r_s.

Hydrophilic particle ($\theta_p = 50°$). Figure 4 illustrates the shape of the air-liquid interface in three different cases of wetting degree of the substrate characterized by contact angles $\theta_s = 100°$ (blue line), $\theta_s = 50°$ (pink line), and $\theta_s = 10°$ (black line). In these examples, the position of the contact line on the substrate is again fixed at $r_s/a = 0.5$. Similar to the case of the hydrophobic particle, the bubble volume decreases with the increase of θ_s, and this is translated into a decrease in pressure difference, Δp ($\Delta p \approx -11 \times 10^5$ Pa for hydrophilic and $\Delta p \approx -7 \times 10^5$ Pa for hydrophobic substrates). Here, we once again varied the substrate contact angle θ_s (from hydrophilic $\theta_s = 2°$ to hydrophobic $\theta_s = 140°$) and the position of the contact line on the substrate, r_s (from $r_s = 0.05$ μm
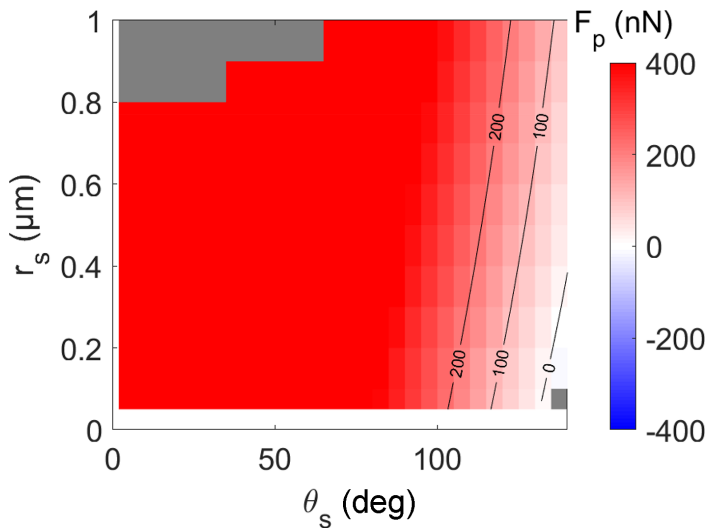

FIG. 5. Map of the force F_p applied by the bubble on the particle. The color code is identical to that of Fig. 3. The particle is hydrophilic with $\theta_p = 50°$.

TABLE I. Advancing, receding, and static contact angles (c.a.) for substrates (two top lines) and the particles (two bottom lines) used in the experiments.

	Materials	Static c.a.	Advancing c.a.	Receding c.a.
θ_s	Piranha-treated glass	2°		
	PFTS-coated glass	100° ± 4°	117°	89°
θ_p	Silver-coated silica	10° ± 4°		
	Polyethylene	125° ± 5°	162°	83°

to $r_s = 1$ μm). Figure 5 shows the F_p map as a function of θ_s and r_s. The color code is identical to that of Fig. 3.

One can see that F_p is almost always directed upward except for a tiny region located on the bottom-right corner of the graph where θ_s has a large value ($\theta_s \gtrsim 135°$) while r_s is small ($r_s \lesssim 0.4$ μm). This means that the presence of a trapped bubble underneath a hydrophilic particle will almost always have a releasing effect on the particle except for strong hydrophobic substrates combined with small bubble volumes.

III. EXPERIMENTS

A. Materials and methods

In this section, we first describe the method used to measure the wetting contact angle of the particles and the substrates. We next detail the procedure for placing and then immersing particles on substrates of various wetting properties. Finally, the experiments that permitted one to estimate the force required to detach a particle from a surface are described.

Two different types of beads were used in our experiments: hydrophilic silver-coated silica microspheres (Cospheric) having a diameter of 2 μm and hydrophobic polydisperse clear polyethylene microspheres (Cospheric) with a particle diameter ranging from 1 to 4 μm. When performing our experiments with the latter particles, we selected those of diameter of about 2 μm. The particle contact angle was measured using the method of placing a droplet on a lawn of particles [19]. Briefly, we passed 1.5 ml of particle suspension through the filter (cellulose esters 0.025 μm) to form a dense lawn of particles. Then, a water droplet was placed on this lawn and the contact angle measured using an optical tensiometer (Biolin Theta Lite) in "sessile drop" mode (to measure static contact angle) and "dynamic contact angle" mode (to measure advancing and receding contact angles). The same optical tensiometer was used to measure the substrate contact angle. The results are presented in Table I. In this study, two different types of substrates were employed: glass treated with a hydrophilic piranha solution and glass coated with a hydrophobic perfluorodecyltrichlorosilane (PFTS) layer. For hydrophilic materials, measurements of advancing/receding angles were not possible due to instantaneous spreading of the droplet over the substrate/lawn. In the table, an important hysteresis can be seen for polyethylene particles. This likely arises from the pillarlike structure of the particle lawn, which promotes hydrophobicity while surface asperities pin the contact line and enhance the hysteresis.

In order to place and immerse the particles on substrates of different wettability, we adopted the following procedure. First, a suspension of microbeads was prepared by dispersing 35 ± 5 μg of dry particles into 500 μl of deionized water. For hydrophobic particles, 30 μl of ethanol was added to the solution to enable their suspension and avoid any particle floating at the liquid-air interface. Next, a droplet of 2 μl of the suspension containing the microspheres was placed onto either a hydrophilic piranha-treated or hydrophobic PFTS-coated glass coverslip. The coverslip was then placed in an oven set to 40 °C for 1 h (typically, a complete evaporation of a 2 μl water drop at 40 °C droplet occurs after 15–20 min). After the removal of the coverslip from the oven and its cooling to room temperature a Hanks' balanced salt solution [20] (HBSS) [21] is gently poured over until the liquid

height is about 3 mm and particles are fully immersed. Finally, the coverslip is placed in a vacuum chamber (Nalgene, volume 4.7 l; vacuum pump Laboport N 86 KN.18) for 10, 20, or 40 min (this step is skipped for experiments without degassing). As per the manufacturer's specifications, the pump achieved the maximum vacuum level of approximately 100 mbar after around 10 min for our 4.7-l vacuum chamber. However, our pressure measurements over time indicated that it took approximately 15 min to reach the targeted vacuum level of 100 mbar. The extended degassing time we incorporated into our experiments was intended to account for the removal of excess gas within the HBSS solution. This procedure was precisely designed to target any trapped bubbles beneath a particle, with the intention of causing them to shrink until they ultimately vanished. After completing the degassing step, the coverslip was gently and gradually returned to atmospheric pressure before being positioned on the patch-clamp setup for measuring particle removal force.

The detachment force is measured using the basis of the patch-clamp technique [22] except the clamping is enabled by means of flow depression instead of voltage difference. In fact, in the classical technique a pipette filled with an electrolyte solution and containing an electrode is brought into contact with a cell located in a bath that shelters a ground electrode. A voltage is typically applied to clamp the cell and an amplifier connected to the electrodes records ionic current of interest to researchers in biology. Here, we only use the electrodes for assessing the electrical resistance of the pipette with the intention of determining its tip size. A monitored flow depression (Fluigent LineUp Flow EZ) is applied through the pipette once its tip is in the extreme close vicinity of the microbead's surface. The pipette is then moved away vertically from the particle at a given speed (3 μm/s). The response of the particle is lively as observed under the microscope. If the particle remains on the substrate, i.e., it does not detach, the micropipette is approached again and a higher aspiration pressure is applied. The experiment is repeated until the particle detaches. From the minimum pressure, allowing the detachment, a force is worked out knowing the surface area of the pipette's tip. This value would then correspond to the minimum force required to remove the particle from the substrate. To generate the detachment curve, a minimum of 30 particles were dislodged from their substrates in the cases of no degassing or 20 min of degassing, and a minimum of 10 particles were dislodged in the cases of 10 or 40 min of degassing. It has to be noted that in order to avoid any collective, neighboring, or side effects on the measurements, we solely selected isolated particles on the substrate.

B. Results

Figure 6 presents the results for experiments carried out on PFTS-coated hydrophobic substrate with hydrophobic (top) and hydrophilic (bottom) particles. The graphs show the percentage of particles (*y* axis) that we have been able to detach with a given applied force (*x* axis). Circles represent the results obtained in experiments conducted without degassing, while triangle, diamond, and square symbols correspond to degassing times of 10, 20, or 40 min, respectively. Figure 7 displays data similar to the previous figure, but for a substrate that has undergone piranha treatment (hydrophilic). A nonlinear least-square fit is performed on the experimental data of Figs. 6 and 7. The fit uses the logistic function

$$y_{\text{fit}}(x) = \frac{100(e^{bx} - 1)}{e^{bx} - c}, \tag{8}$$

where $b > 0$ and c are fitting parameters, x is the applied force (in nanonewtons), and y_{fit} is the percentage of removed particles at a corresponding applied force x. A mean detachment force associated with the probability of removing up to 50% of the particles is calculated from the fitted curve and is presented in Table II.

From Fig. 6, which illustrates data collected using a hydrophobic substrate ($\theta_s = 100°$), several observations can be made. First, the results show that prior to degasification, the value of the detachment force, F_d, is larger for hydrophilic than for hydrophobic particles (cf. Table II for detailed values at 50%). This is probably due to the size of the bubble that can be trapped with
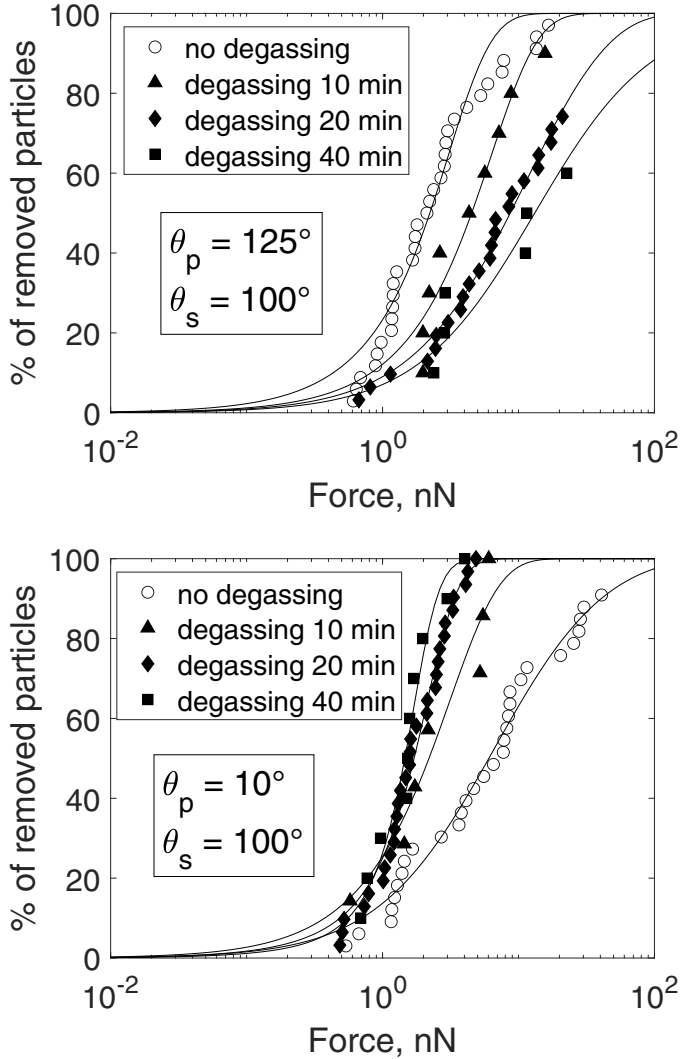
FIG. 6. Experimental curves obtained for hydrophobic (top) and hydrophilic (bottom) particles placed onto hydrophobic substrate. The solid lines depict the fitting lines using the logistic equation, Eq. (8).

respect to the wetting properties of the surfaces when immersing the system. Second, while the value of F_d decreases with degasification for hydrophilic particles, it increases for hydrophobic particles. This change in F_d value with degasification indirectly demonstrates the presence of bubbles underneath the particles in these systems. Third, the amount of degassing time, $\Delta\tau$, seems to nonequivalently affect these two systems. In the case of hydrophilic particles, F_d remains more or less constant around a value of $F_d \sim 2$ nN regardless of $\Delta\tau$ as long as a first degasification has taken place. In the case of hydrophobic particles, there is a steady increase in F_d from 2.2 to 13.2 nN with $\Delta\tau$. In other words, for an identical hydrophobic substrate, the degasification facilitates or restrains the removal of particles upon their hydrophilic or hydrophobic characteristics, respectively.

Experimental data obtained with a hydrophilic substrate ($\theta_s = 2°$) are shown in Fig. 7. Similar to the previous paragraph, we hereafter cite remarkable observations. First, for hydrophobic particles, the order of magnitude of the 50% detachment force is about a few nanonewtons, which is similar
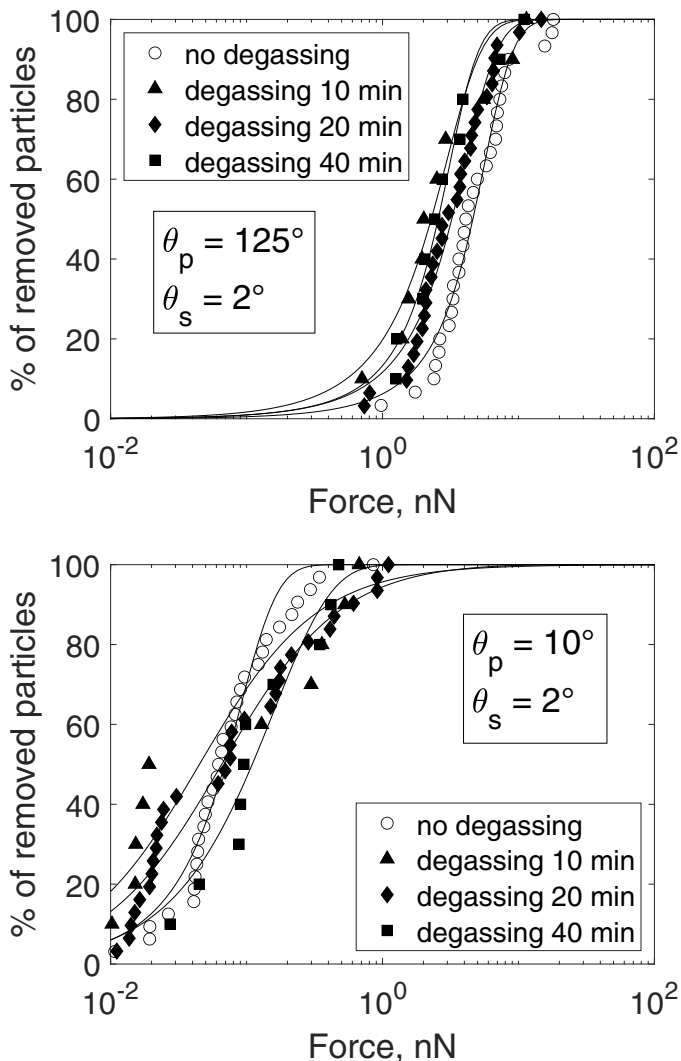
FIG. 7. Experimental curves obtained for hydrophobic (top) and hydrophilic (bottom) particles placed onto hydrophilic substrate. The solid lines depict the fitting lines using the logistic equation, Eq. (8).

to experiments carried out with hydrophobic substrates at least for low degassing levels. Second, experiments carried out with both surfaces—particles and substrate—hydrophilic, show a 50% detachment force of the order of 10^{-2} nN (cf. Table II). This is a much lower value in F_d compared to any other combination of wettability for the involved particle/substrate surfaces that yielded until now a F_d of the order of 1 nN. It has to be noted that the measurement of forces of the order of 10^{-2} nN was at the limit of the present patch-clamp technique and could result in reduced accuracy. Third, the degasification seems to have minor or no effect on F_d in the experiments carried out with hydrophilic particles. Indeed, the detachment force variations given in Table II can be presumed constant considering the data scatter at the limit of the patch-clamp technique (Fig. 7, bottom). The absence of effect from the degasification combined with the low value of F_d for hydrophilic surfaces, may suggest the absence of a trapped bubble. Fourth, in the case of hydrophobic particles,

TABLE II. Mean detachment forces obtained from fitting curves, Eq. (8), and corresponding to experiments without or with degassing for 10, 20, or 40 min. Data for various combinations of hydrophobic (PFTS coated, $\theta_s = 100°$) and hydrophilic (pirahna cleaned, $\theta_s = 2°$) substrates with respect to particle wetting characteristics ($\theta_p = 125°$ and $\theta_p = 10°$).

	Case	0 min	10 min	20 min	40 min
Hydrophobic substrate, $\theta_s = 100°$	Hydrophobic particle, $\theta_p = 125°$	2.2 nN	4.5 nN	8.7 nN	13.2 nN
	Hydrophilic particle, $\theta_p = 10°$	6.1 nN	2.2 nN	1.7 nN	1.5 nN
Hydrophilic substrate, $\theta_s = 2°$	Hydrophobic particle, $\theta_p = 125°$	4.6 nN	2.3 nN	3.2 nN	2.6 nN
	Hydrophilic particle, $\theta_p = 10°$	0.07 nN	0.05 nN	0.07 nN	0.11 nN

F_d remains more or less constant around an average value of $F_d \sim 2.7$ nN regardless of $\Delta\tau$ as long as a first degasification has taken place.

When looking at all experimental results (Table II), it appears that the order of magnitude of the detachment force is set higher as long as one of the involved surfaces is hydrophobic. The degasification can have an initial effect but shortly becomes insensitive to increasing $\Delta\tau$ if one of the surfaces has opposite hydrophobicity. Finally, the effect of degasification, hence a change in bubble volume, is particularly striking when both surfaces are hydrophobic.

The experiments through the difference in the measured detachment force strongly suggest the existence of a bubble when at least one of the surfaces, i.e., the particle or the substrate, is showing hydrophobic characteristics—the extremely low values of this force for exclusively hydrophilic surfaces may indicate the absence of a bubble, although that assertion could not be verified experimentally with our equipment. Without considering the presence of a trapped bubble, a physical explanation of the variation in this force with the degassing would be hard and puzzling. Indeed, the degassing promotes at least the shrinking of the bubble size or at best its vanishing. One would then expect a change in the detachment force as observed in the experiments if a bubble is trapped under a microparticle. The variation of this force with the degasification is the signature of the presence of a trapped bubble. However, the scenario of bubble shrinking or vanishing can be complex from the fact that the system is put in a vacuum for degasification and had to be brought back to the atmospheric pressure for measuring the detachment force in the patch-clamp setup. The effects of these experimental steps on the measured force will be discussed in the next section.

IV. DISCUSSION

Looking at the experimental F_d values for a hydrophobic particle on hydrophobic substrate in Table II, a good agreement with the numerical calculations (Figs. 3 and 5) can be observed. Indeed, for $\theta_p = 125°$ and $\theta_s = 100°$ the calculations show that the presence of the bubble brings an extra force to further retain the particle on the substrate regardless of the size of the bubble, i.e., the value of r_s, compared to a case without any bubble. This observation was verified experimentally where the value of measured F_d is higher for this combination of $\theta_p = 125°$ and $\theta_s = 100°$. More interestingly, by decreasing r_s, i.e., by decreasing the size of the bubble, the value of F_d increases. This is in full agreement with the experimental observations where the shrinking bubble size with degasification comes with an increase in F_d. However, the agreement remains good on the overall behavior but limited on the value of F_d, which is found of the order of 100 nN for the numerical model, whereas it is about 10 nN for the experiments. Indeed, care should be taken when comparing these results: the numerical model only takes into account forces arising solely from the presence of the bubble whereas the measured forces in the experiment reflect also the particle-substrate interactions. Therefore, the difference found in F_d values in the experiments compared to simulations is not contradictory to the model. However, for the computed case ($\theta_p = 125°; \theta_s = 100°$) where the force

due to the bubble appears to be relatively large ($F_p \sim O(100 \text{ nN})$), one would have expected the latter to overshadow the force arising from the substrate-particle interactions. This does not seem to occur with respect to measured experimental values of $F_d \sim O(1 - 10 \text{ nN})$.

For the computational case of ($\theta_p = 125°$; $\theta_s = 2°$), the differences even cumulate where a shrinking bubble gives a decrease in F_p in the experiments while it increases in the model. The possible roots of these differences will be discussed later in the section.

Regarding the other numerical calculations tested with a hydrophilic particle ($\theta_p = 50°$; Fig. 5), the results properly emulate the experimental observations where the bubble facilitates the detachment regardless of the substrate's contact angle. At small θ_s the positive contribution of this extra force reaches its highest values and this also corresponds to the lowest values of F_d measured experimentally. For larger θ_s values above $90°$, i.e., when the substrate becomes hydrophobic, the numerical model shows a bubble size dependency. In this case the positive contribution of bubble force F_p decreases and may even become null with decreasing r_s. However, this is not translated in the experiments with an increase but with a decrease in F_d for $\theta_p = 10°, \theta_s = 100°$.

As mentioned, the numerical calculations show only a partial agreement with the experimental results and we may now describe their possible causes. First, the numerical model considers a symmetrically placed bubble under the particle. This, of course, is rarely achievable in a real system and could be part of the source of the differences. Second, the model considers ideal smooth surfaces whereas such system does not exist in reality. As a consequence, the local contact angle for either θ_p or θ_s may not correspond to static contact angles that we assumed numerically. This will also bring asymmetry of the contact angle along the contact line between the bubble and either the particle and/or the substrate. Third, the effect of nonideality of the surfaces in contact with the bubble may well become more pronounced during the degasification stages in the experiments we are now going to describe.

Initially, the air bubble, in the state "0," can be characterized by its pressure p_{A0}, volume V_{A0}, the position of its contact line on the substrate r_{s0}, and the contact angles with the particle θ_{p0} and the substrate θ_{s0}. With the degasification, one expects the bubble to lose some of its substance or, in the least favorable case, keep its initial characteristics. Within the ideal gas approximation, this translates to

$$p_{A0}V_{A0} \geqslant p_{A1}V_{A1}, \tag{9}$$

with the subscript "1" designing the final state after the degasification. In the following paragraphs, we will describe two distinct transformations that the bubble may undergo during the degasification. The first will consist of a modification in the surface contact angle due to, for instance, the wetting hysteresis. The second is a change in the bubble's volume that may arise from the depinning of the contact line during the degasing phase. Note that in the real system, a complex combination of these two events may occur simultaneously but will not be addressed here.

If the positions of the contact lines on the substrate and the particle are locked up, i.e., contact lines are pinned, any change in pressure will automatically induce a shape modification, and consequently, a change in θ_p and θ_s values. Of course, in the assumption of an axisymmetric placement of the bubble throughout this study, any change in θ_p and θ_s will also modify the volume.

In the case of a decrease in bubble volume while the wetting properties are conserved, i.e., $\theta_{p1} = \theta_{p0}$ and $\theta_{s1} = \theta_{s0}$, the behavior of the detachment force in this situation would essentially depend on the final position of the contact line on the substrate, r_{s1}. The system behavior can be figured out from the numerical model by referring, for instance, to low values of r_s in Fig. 3 for the case of a hydrophobic particle. As can be seen inthe figure for values of θ_s larger than approximately $55°$, a decrease in r_s would imply a smaller or even a negative F_p, which means one has to apply a larger force F_d to detach the particle from the substrate. This is in agreement with the experiments where in Table II one can observe that the degasification of the system having both surfaces hydrophobic (particle and substrate) yields a larger detachment force.

Although the agreement with experiments appears to support the above physical explanation, one must be reminded of the possible coexistence of an alternative scenario where the contact angles

can also vary due to the hysteresis. Indeed, prior to patch-clamp experiments run under atmospheric pressure, the degasification step may induce a temporary enlargement of the bubble. This causes a complication on the final bubble state where one, or both, contact lines (θ_p, θ_s) may remain pinned on their positions acquired during the degasification. As a consequence, one would expect in the final state either a larger r_s value and/or a larger contact angle on one or both surfaces. In order to find the configuration that could match our experimental observations (Table II), we carried out numerical computations. The effect of degasification on the detachment force through a modification of the contact angles and/or on the substrate position r_s was investigated. This was done by varying the control parameters $(\theta_p, \theta_s,$ and $r_s)$ around their mean values and for different surface hydrophobicity. For these calculations, the substrate position was set to $r_s = 0.5\,\mu\text{m}$ while the values of θ_p and θ_s used those of measured values of Table I except for $\theta_p = 10°$. Indeed, as mentioned before, due to numerical limitations, for low values of the particle contact angle, we set the latter to $\theta_p = 50°$. Even though this numerical value is higher, it still represents a hydrophilic characteristic of the particle and can enlighten us about the main behavior of the system. We would like to emphasize that the calculations failed to produce mathematical solutions for the scenario involving a hydrophobic particle and a hydrophobic substrate. Consequently, these results are not presented in the following sections.

Figures 8(a)–8(c) show three different maps corresponding to various combinations of particle/substrate wetting properties that were tested in the experiments (cf. Table I). The initial state is highlighted by a central black star around which the three parameters are varied. Four regions are represented in different colors corresponding to the following conditions: (i) $F_{d1} < F_{d0}$ and Eq. (9) not valid (light blue); (ii) $F_{d1} \geqslant F_{d0}$ and Eq. (9) not valid (dark blue); (iii) $F_{d1} < F_{d0}$ and Eq. (9) valid (pink); and finally (iv) $F_{d1} \geqslant F_{d0}$ and Eq. (9) valid (purple). In the maps, the isolines show the additional force that the system will need in order to detach the particle from the substrate. To avoid any confusion, it is important to clarify that when an isoline is negative, it indicates that a higher detachment force is required to dislodge the particle from the substrate. The area with no physical solution (i.e., $p_A < 0$) is gray colored.

Figure 8(a) represents the map of a hydrophobic particle $(\theta_p = 125°)$ over a hydrophobic substrate $(\theta_s = 100°)$. According to the experimental results (Table II), the mean force increases with degasification for this set combination of $(\theta_p = 125°; \theta_s = 100°)$. In this regard and with respect to the condition, Eq. (9), only the purple region should be considered where an increase in the detachment force corresponds to the area of negative isoline values. Although the maps do not provide a firm affirmation of the way the system behaves exactly, i.e., which of the three parameters contributes to the increase of the experimentally observed F_d, it at least indicates in which direction the system is probably heading. With the present map, it shows the region where the combined variations in r_s, θ_s, or θ_p can satisfy and agree with the experimental observation (purple region). In the figure, black solid arrows indicate possible variations in r_s and θ_s, while black dashed arrows show variations of θ_p. As observed, a significant rise in F_d, indicated by the transition towards negative isolines, can occur with minor variations in r_s and θ_s. However, a noticeable increase in F_d with a change in θ_p is not readily observable. This is indicated by a weak negative slope, implying that an increase in F_d is only achievable through a decrease in θ_p. These findings suggest that a decrease in θ_s may be one of the primary factors associated with contact line hysteresis, thereby contributing to the observed increase in F_d in the experiments involving degasification.

Similarly, the maps depicted in Figs. 8(b) and 8(c) illustrate the outcomes when the particle and substrate exhibit opposite wettability, characterized by contact angle pairs of $(\theta_p = 125°; \theta_s = 2°)$ and $(\theta_p = 50°; \theta_s = 100°)$. The experimental findings regarding degasification demonstrate a reduction in the F_d value (see Table II). In the current map, the pink shade emphasizes this trend, where $F_{d1} \leqslant F_{d0}$, and the validity of Eq. (9) persists. To recall, in Fig. 8, the solid and dashed arrow lines respectively represent variations in r_s and θ_s on one side, and θ_p on the other. In Fig. 8(b), it is evident that a decrease in the detachment can only be attained by reducing θ_p regardless of any potential changes in r_s or θ_s. This observation implies that a hysteresis phenomenon occurs for θ_p in experiments where the particle is hydrophobic and the substrate is hydrophilic. Conversely, in
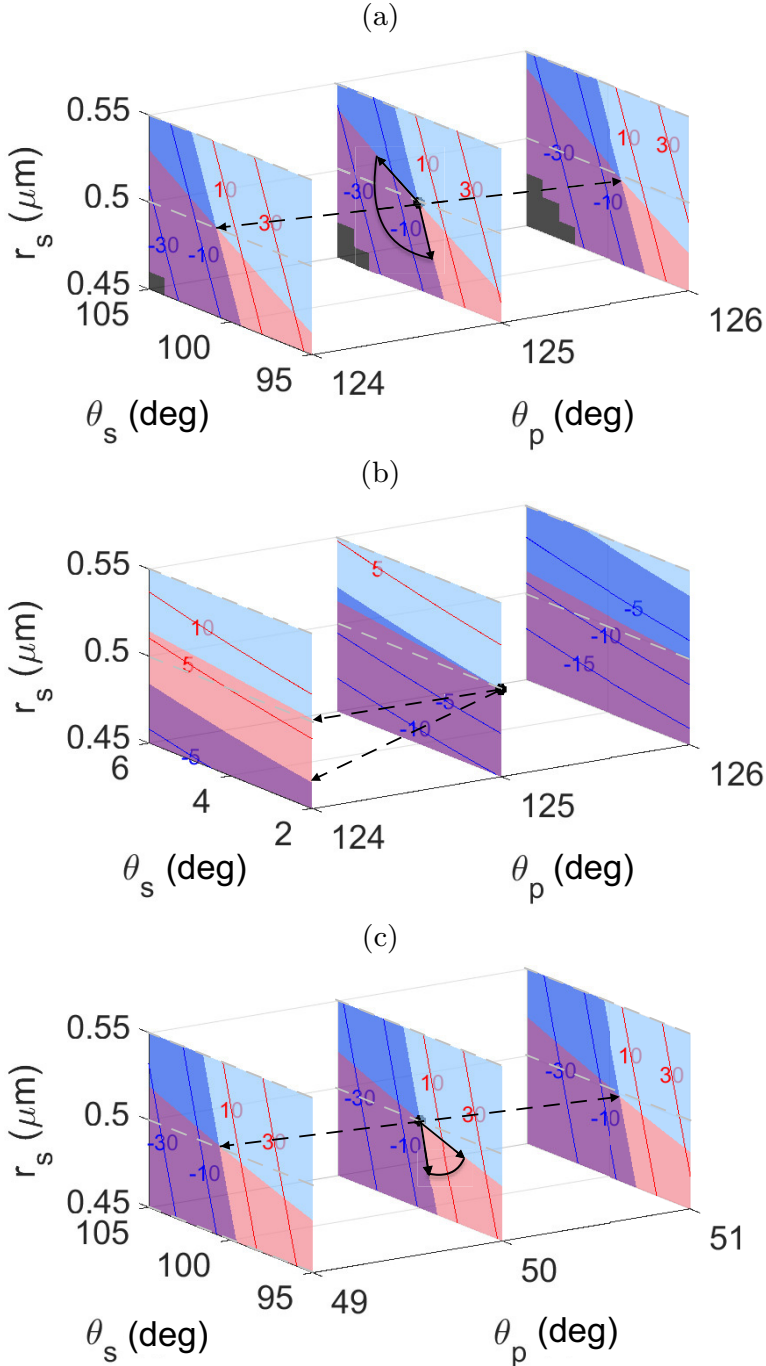
FIG. 8. Map of bubble states for different initial states: $(\theta_{s0} = 100°, \theta_{p0} = 125°)$ (top); $(\theta_{s0} = 2°, \theta_{p0} = 125°)$ (middle); $(\theta_{s0} = 100°, \theta_{p0} = 50°)$ (bottom). For all the cases, $r_{s0}/a = 0.5$. The isolines illustrate the extra force (in nanonewtons) relative to the initial state (marked with a black star). They illustrate how slight variations in θ_p and θ_s could result in an additional attraction (negative values) or repulsion (positive values) force between the particle and the substrate. The solid and dashed arrow lines respectively indicate variations in r_s and θ_s on one side, and θ_p on the other.
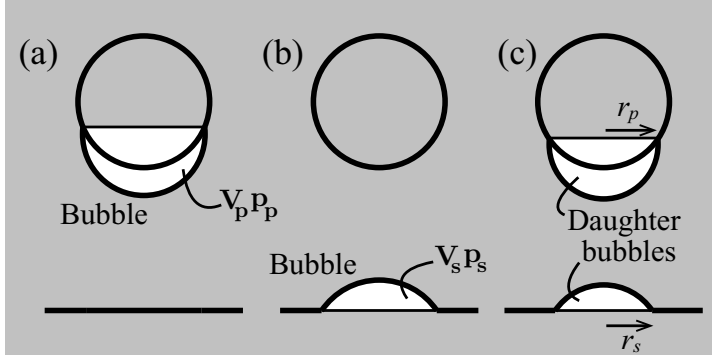
FIG. 9. Configurations of bubbles after the detachment of a particle. (a) Detachment with bubble, (b) detachment without bubble, and (c) mixed case.

the case of a hydrophilic particle and a hydrophobic substrate [Fig. 8(c)], variations in θ_p appear to have little effect on the system (indicated by a very weak slope), while θ_s must decrease to facilitate a lower detachment force. This suggests that the hysteresis occurs primarily on the substrate. Upon examining Figs. 8(b) and 8(c), it becomes evident that hysteresis occurs predominantly on the most hydrophobic surface.

The simulations mentioned above demonstrate that slight variations in θ_p, θ_s, or r_s can result in detachment force variations comparable in magnitude to those observed in experiments. The results imply that hysteresis may indeed be present in the experiments, either on the surfaces of the particle or on the substrate, or possibly on both, for other combinations of wall wetting characteristics that were not examined in this study. This observation could provide an explanation for the disparities observed between computational and experimental findings.

Another interesting question about the particle detachment against the adhesion force due to a bubble is the state of the bubble after the particle is removed from the substrate surface. Three possible configurations can be identified for particle detachment: (i) a detachment with the entire bubble [Fig. 9(a)], (ii) a detachment without the bubble [Fig. 9(b)], or (iii) a mixed case where the bubble splits between the particle and the substrate [Fig. 9(c)].

We could infer the particle state by an energetic consideration on the total energy U of a stationary particle-bubble system,

$$U = \gamma(A_{Lp} + A_{Op} \cos \theta_p) + \gamma(A_{Ls} + A_{Os} \cos \theta_s) + U_{\text{ref}}, \tag{10}$$

where A_L and A_O stand, respectively, for the areas of liquid-gas and liquid-solid interfaces. The subscripts p and s indicate to which solid surface, either particle (p) or substrate (s), the quantities are concerned with. Thereafter, we may use the subscript i to design either of these two surfaces i ($= p, s$). The energy U_{ref} refers to the system with no bubble, which we take as a reference.

For a specified surface tension γ, fixed contact angles θ_p and θ_s, and a given particle radius a, the energy U solely depends on the radii r_p and r_s of the bubble on the particle and the substrate [as depicted in Fig. 9(c)]. This relationship is expressed as $U = U(r_p, r_s)$, since the areas A_L and A_O are geometrically linked to these radii as well as to θ_p and θ_s. On the other hand, assuming that bubbles contain noncondensable gas only, they are subject to the mass conservation:

$$p_p V_p + p_s V_s = p_0 V_0, \tag{11}$$

where p_i and V_i represent the pressure and volume of the bubble on the solid surface, with the subscript i ($= p, s$) indicating whether it is associated with the particle (p) or the substrate (s) (see Fig. 9). The volumes V_p and V_s only depend on, respectively, (a, θ_p, r_p) and (θ_s, r_s). The volume V_0 is that of the given amount of gas when it is maintained at the surrounding pressure p_0. The

bubble pressure p_i is connected to the pressure p_0 through the pressure balance at the interface: $p_i - \frac{2\gamma}{R_i} = p_0$, where R_i denotes the radius of the bubble attached to either the particle (R_p) or the substrate (R_s). Thus, for a given ($\gamma, \theta_p, \theta_s, a$), Eq. (11) represents a relationship between r_p and r_s that has to satisfy the mass conservation and can be rewritten as

$$\Phi(r_p, r_s) := p_p V_p + p_s V_s - p_0 V_0 = 0. \tag{12}$$

Seeking the radius values ($r_{p,\min}, r_{s,\min}$) minimizing U, Eq. (10), under the constraint (12), we can infer the representative configuration after the particle detachment: if $r_{s,\min} = 0$, the bubble detaches from the substrate with the particle [Fig. 9(a)]; if $r_{p,\min} = 0$, the bubble remains at the substrate [Fig. 9(b)]; if neither $r_{s,\min}$ nor $r_{p,\min}$ vanish, two daughter bubbles are attached to both the particle and the substrate [Fig. 9(c)]. Figures 10(a) and 10(b) summarize in two maps the values of, respectively, $r_{p,\min}$ and $r_{s,\min}$ in the θ_p-θ_s plane for a given ($a, \gamma, p_0, p_0 V_0$). These maps were computed for the ratio of liquid to capillary pressure of $p_0 a/\gamma = 2$ and the bubble-particle size ratio $p_0 V_0/\gamma a^2 = 0.4$. In these maps, the gray area indicates $r_p = 0$ in Fig. 10(a) and $r_s = 0$ in Fig. 10(b). They respectively represent the situations illustrated in Figs. 9(b) and 9(a). The configuration of Fig. 9(c) with the presence of daughter bubbles can be easily worked out by taking the difference of the two maps of Figs. 10(a) and 10(b). The red lines in Fig. 10 indicate the wetting characteristics explored in the experiments. For hydrophobic particles $\theta_p = 125°$, it appears that for the tested substrate values $\theta_s = 2°, \theta_s = 100°$, the system would show a bubble fully sticking to the particle in the detachment process. For hydrophilic particles $\theta_p = 10°$, in contrast, we have $r_p = 0$, i.e., the entire bubble remains on the substrate after the detachment. These suggested bubble configurations following particle detachment are important in the context of surface cleaning, as the interaction of particles with adjacent solid surfaces can be influenced by the presence of bubbles.

The energetic consideration presented above remains of qualitative nature. The radii r_p and r_s minimizing the energy U depends on the dimensionless pressure $p_0 a/\gamma$ and the dimensionless amount of air $p_0 V_0/\gamma a^2$. However, we have no access to the latter information by the present experiment for comparison. Furthermore, the theory does not take into account the dynamics during the particle detachment that may also affect the final bubble configuration. These points would be considered by future theoretical and experimental work.

Assuming static equilibrium at all times, the minimum energy, $U_{\min}$, of the separated equilibrium state according to (10) allows one to predict the final state of the system after particle detachment, which is the main objective of our paper. The remaining task is to determine how this state can be reached, i.e., the necessary particle displacement and the minimum force required throughout this process. This can be achieved by modifying expression (1) for the particle force, F_p, to account for the vertical wall distance of the particle center, z_p. The resulting modified expression, $\widetilde{F}_p(z_p)$, is valid for $z_p \geqslant a$, and can be used to make two predictions.

Firstly, the work needed to displace the particle to a certain distance, $z_p = d$, can be determined by integrating $\widetilde{F}_p(z_p)$ with respect to z_p, from $z_p = a$ to $z_p = d$. This allows us to establish a relationship between the initial energy of the system, denoted as $U(r_p, r_s)$, the work required for vertical particle displacement, and $U_{\min}$:

$$U(r_p, r_s) + \int_a^{d_{\min}} \widetilde{F}_p(z) dz = U_{\min}, \tag{13}$$

where $d_{\min}$ is the particle distance at which the energy of the unseparated equilibrium state reaches $U_{\min}$. This distance needs to be confronted with the minimum distance, d_{crit}, at which the minimum-energy separated state is geometrically possible (no mutual exclusion of the gas bubbles attached to the particle and wall). For $d_{\min} < d_{\text{crit}}$, the minimum-energy separated state is not yet geometrically possible, and more work needs to be performed to separate the initial gas bubble. This excess work will eventually dissipate as the separated gas bubble relaxes to its minimum-energy equilibrium. Conversely, for $d_{\min} \geqslant d_{\text{crit}}$, the bubble will separate when reaching $U_{\min}$ at $d = d_{\min}$ with no dissipation. Thus, the particle distance at which the bubble separates, $\hat{d}$, is either $\hat{d} = d_{\text{crit}}$, where
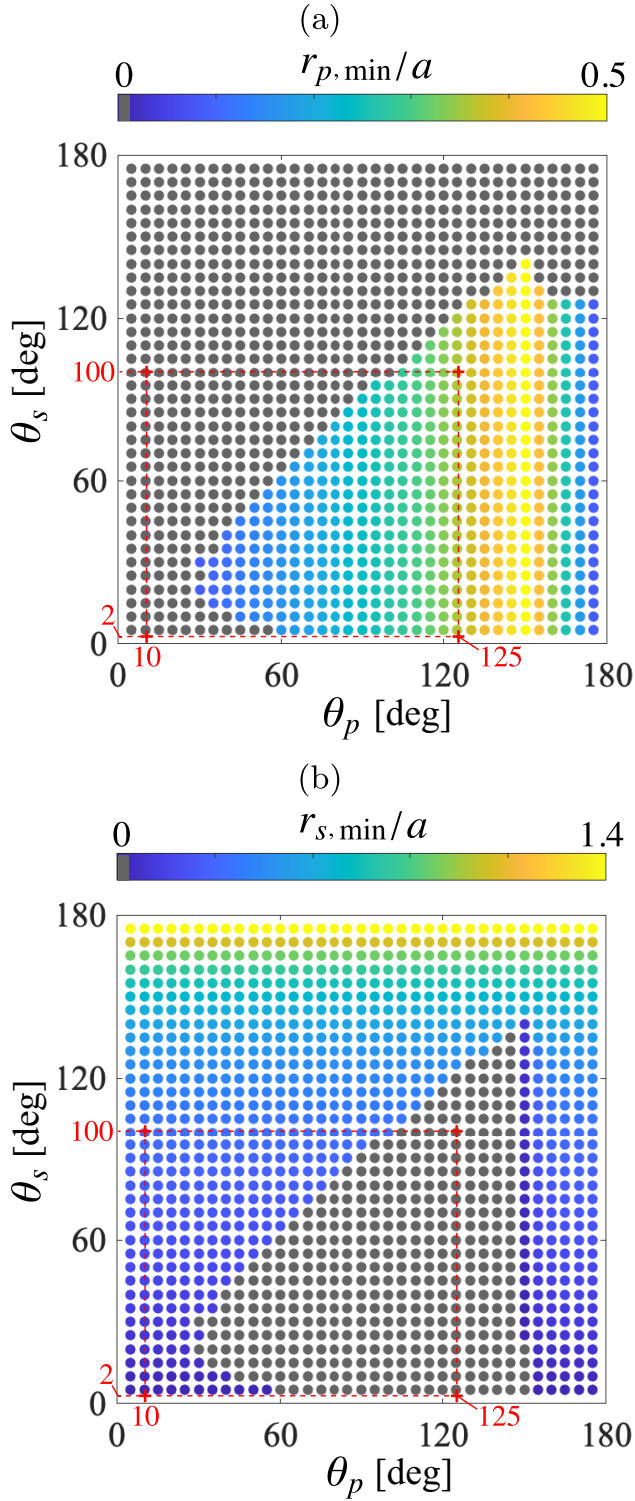
FIG. 10. Bubble foot radii $r_{p,\min}$, $r_{s,\min}$ minimizing the surface energy U for $p_0 a/\gamma = 2$, $p_0 V_0/\gamma a^2 = 0.4$.

d_{crit} is obtained from the particular geometry of the minimum-energy separated state ($U = U_{\text{min}}$), or $\hat{d} = d_{\text{min}}$, where d_{min} is obtained from (13).

Secondly, by evaluating $\widetilde{F}_p(z_p)$ across the integration path from $z_p = a$ to $z_p = \hat{d}$, one can determine the necessary force history for a virtual quasistatic detachment experiment. Thus, if the particle force applied in a real experiment is greater at all times than the maximum of $\widetilde{F}_p(z_p)$ for $a \leqslant z_p \leqslant \hat{d}$, detachment is certain.

V. CONCLUSION

We investigated the possible presence of an air bubble trapped between a particle and a substrate. A theoretical model supplemented by its companion numerical calculation gave access to values of bubble-induced forces with respect to various surface wetting characteristics. Specifically, the computational findings indicated that, in most cases, the presence of a trapped bubble beneath a hydrophilic particle enhances the likelihood of particle detachment, with the exception being strong hydrophobic substrates when combined with small bubble volumes. When dealing with hydrophobic particles, the impact on particle detachment was observed to be contingent on both the wetting properties of the substrate and the size of the bubble, leading to either a positive or a negative effect. In line with the numerical findings, experimental tests were conducted with the primary aim of confirming the existence of the bubble. This was achieved by comparing detachment force measurements with and without a degasification step preceding the measurement. The noticeable change in the measured force as a result of degasification provided clear evidence of the presence of a trapped bubble. Comparison between computations and experiments showed a partial agreement on the overall behavior but differed on the magnitude of the found detachment force. Various hypotheses were put forward to account for these differences. Notably, it was conjectured that they could be attributed to the nonideality of the surfaces (roughness) and the nonsymmetric placement of the bubble during the particle immersion process. Finally, a theoretical model based on energy considerations was introduced. It offered insights into potential scenarios when the particle detaches, including instances in which the bubble could adhere to the particle, the substrate, or both.

The present study showed that a bubble can be trapped under a particle if at least one of the involved surfaces in the system, i.e., that of the particle or the substrate, is hydrophobic. However, this entrapment appears unlikely when all surfaces are hydrophilic. This result is of particular interest to, for instance, food industries where the contamination of surfaces of food processing lines by pathogens and spoilage bacteria is a major issue that has not yet found a proper cleaning and disinfection solution. Knowing that bacteria can present different degrees of hydrophobicity [23], the surface treatment with a judicious coating with respect to the wetting properties of the potential pathogens, can greatly facilitate the bacterial removal. Engineering surface coating with respect to the type of bacteria would ease their detachment and prevent the further overuse of chemicals for equipment disinfection and, therefore, contribute to the implementation of greener industrial processes.

APPENDIX A: NUMERICAL PROCEDURE

Semianalytic solution of the boundary value problem (4) with boundary conditions (5) and (6) was proposed by Orr *et al.* [17] in 1975. In this work, we solve the problem numerically using a
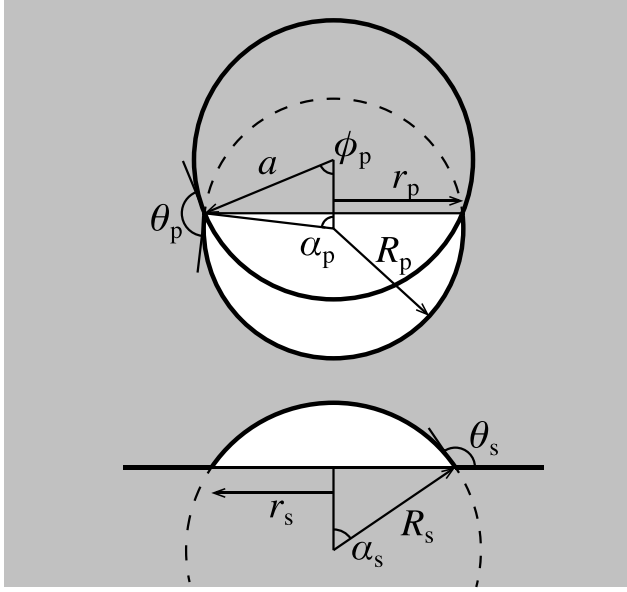
FIG. 11. Definitions of the geometries of two bubbles after the detachment of a particle.

shooting method. First, we choose r_s, for which we search for the solution. For the kth iteration, we use $\Delta p^{(k-1)}$ [obtained from the $(k-1)$th iteration or supposed, if $k=0$] to integrate Eq. (4) with the boundary conditions (5). The integration stops when the solution crosses the particle at some point. At this point, we calculate the filling angle φ and $\psi(\Delta p^{(k-1)}) = f_z + \cot(\theta_p - \varphi)$, which corresponds to the boundary condition at the particle surface (6). To find a root of $\psi(\Delta p) = 0$, we use Newton's method. Such pressure difference, $\Delta p^{(n)}$, satisfying $|\psi(\Delta p^{(n)})| < \varepsilon$ and $|\Delta p^{(n)} - \Delta p^{(n-1)}| < \varepsilon$, is the required pressure difference, and the corresponding $f(z)$ describes the meniscus shape. We repeat the same procedure for a wide range of r_s, as the experimental r_s is unknown.

APPENDIX B: ENERGY ANALYSIS MODEL

The total energy U of a stationary particle-bubble system illustrated in Fig. 11 is given by

$$U = \gamma A_{Lp} + \gamma_{Op} A_{Op} - \gamma_{Lp} A_{Op} + \gamma A_{Ls} + \gamma_{Os} A_{Os} - \gamma_{Ls} A_{Os} + U_{\mathrm{ref}}, \tag{B1}$$

where the surface energy densities of wet and dry solid surfaces are denoted by γ_L and γ_O, respectively. Invoking the Young-Dupré equations, $\gamma_{Op} - \gamma_{Lp} = \gamma \cos\theta_p$ and $\gamma_{Os} - \gamma_{Ls} = \gamma \cos\theta_s$, we cast Eq. (B1) into Eq. (10)

For a given surface tension γ, given contact angles θ_p and θ_s, and a given radius of particle a, the energy U and the mass conservation constraint $\Phi = 0$ depend only on the radii r_p and r_s of the bubble on the particle and the substrate, as the areas A_{Li} and A_{Oi} $(i = p, s)$ and volumes V_p and V_s relate to $(a, r_p, r_s, \theta_p, \theta_s)$ by geometrical relationships,

$$A_{Lp} = 2\pi R_p^2 (1 + \cos\alpha_p), \quad A_{Op} = 2\pi a^2 (1 - \cos\phi_p), \tag{B2}$$

$$A_{Ls} = 2\pi R_s^2 (1 - \cos\alpha_s), \quad A_{Os} = \pi R_s^2 \sin^2\alpha_s, \tag{B3}$$

$$V_p = \frac{\pi R_p^3}{3}(1 + \cos\alpha_p)^2(2 - \cos\alpha_p) - \frac{\pi a^3}{3}(1 - \cos\phi_p)^2(2 + \cos\phi_p), \tag{B4}$$

$$V_s = \frac{\pi R_s^3}{3}(1 - \cos\alpha_s)^2(2 + \cos\alpha_s), \tag{B5}$$

where R_p, R_s, α_p, α_s, and ϕ_p are geometrical parameters defined in Fig. 11 and given by $R_p = r_p/\sin\alpha_p$, $R_s = r_s/\sin\alpha_s$, $\alpha_p = \theta_p - \phi_p$, $\alpha_s = \pi - \theta_s$, and $\phi_p = \sin^{-1}(r_p/a)$.

---

[1] H. F. Okorn-Schmidt, F. Holsteyns, A. Lippert, D. Mui, M. Kawaguchi, C. Lechner, P. E. Frommhold, T. Nowak, F. Reuter, M. B. Piqué, C. Cairos, and R. Mettin, Particle cleaning technologies to meet advanced semiconductor device process requirements, ECS J. Solid State Sci. Technol. **3**, N3069 (2014).

[2] D. W. Cooper, Particulate contamination and microelectronics manufacturing: An introduction, Aerosol Sci. Technol. **5**, 287 (1986).

[3] F. Tardif, A. Danel, and O. Raccurt, Understanding of wet and alternative particle removal processes in microelectronics: Theoretical capabilities and limitations, J. Telecommun. Inf. Technol. **1**, 11 (2005).

[4] R. A. Bowling, An analysis of particle adhesion on semiconductor surfaces, J. Electrochem. Soc. **132**, 2208 (1985).

[5] Y. Taga, Recent progress in coating technology for surface modification of automotive glass, J. Non-Cryst. Solids **218**, 335 (1997).

[6] K. Bewilogua, G. Bräuer, A. Dietz, J. Gäbler, G. Goch, B. Karpuschewski, and B. Szyszka, Surface technology for automotive engineering, CIRP Ann. **58**, 608 (2009).

[7] M. Mauermann, U. Eschenhagen, T. Bley, and J. P. Majschak, Surface modifications – Application potential for the reduction of cleaning costs in the food processing industry, Trends Food Sci. Technol. **20**, S9 (2009).

[8] M. Basso, M. Simonato, R. Furlanetto, and L. De Nardo, Study of chemical environments for washing and descaling of food processing appliances: An insight in commercial cleaning products, J. Ind. Eng. Chem. **53**, 23 (2017).

[9] J. M. Vicaria, E. Jurado-Alameda, O. Herrera-Márquez, V. Olivares-Arias, and A. Ávila-Sierra, Analysis of different protocols for the cleaning of corn starch adhering to stainless steel, J. Cleaner Prod. **168**, 87 (2017).

[10] M. W. L. Chee, T. V. Ahuja, R. K. Bhagat, N. Taesopapong, S. A. Wan, R. L. Wigmore, and D. I. Wilson, Impinging jet cleaning of tank walls: Effect of jet length, wall curvature and related phenomena, Food Bioprod. Process. **113**, 142 (2019).

[11] I. P. Parkin and R. G. Palgrave, Self-cleaning coatings, J. Mater. Chem. **15**, 1689 (2005).

[12] B. Bhushan, Y. Jung, and K. Koch, Self-cleaning efficiency of artificial superhydrophobic surfaces, Langmuir **25**, 3240 (2009).

[13] M. Nosonovsky and B. Bhushan, Biomimetic superhydrophobic surfaces: Multiscale approach, Nano Lett. **7**, 2633 (2007).

[14] B. Bhushan, Biomimetics: Lessons from nature–an overview, Philos. Trans. R. Soc. A **367**, 1445 (2009).

[15] S. N. Omenyi, J. Chappuis, and A. W. Neumann, Adhesion of small spherical particles to substrates immersed in liquids, J. Adhes. **13**, 131 (1981).

[16] M. B. Ranade, Adhesion and removal of fine particles on surfaces, Aerosol Sci. Technol. **7**, 161 (1987).

[17] F. M. Orr, L. E. Scriven, and A. P. Rivas, Pendular rings between solids: Meniscus properties and capillary force, J. Fluid Mech. **67**, 723 (1975).

[18] S. Aramrak, M. Flury, and J. B. Harsh, Detachment of deposited colloids by advancing and receding air–water interfaces, Langmuir **27**, 9985 (2011).

[19] C. Faille, C. Lemy, A. Allion-Maurer, and F. Zoueshtiagh, Evaluation of the hydrophobic properties of latex microspheres and bacillus spores. Influence of the particle size on the data obtained by the math method (microbial adhesion to hydrocarbons), Colloids Surf., B **182**, 110398 (2019).

[20] HBSS solution is commonly used as a buffer system in cell culture media to aid in maintaining the osmetic pressure and the optimum physiological pH for cellular growth. It is composed of (in millimoles): 142 NaCl, 5.6 KCl, 1 CaCl$_2$, 1 MgCl$_2$, 10 HEPES, 2 NaHCO$_3$, 0.44 KH$_2$PO$_4$, 0.34 Na$_2$HPO$_4$ with an osmolarity of 300 mOsm/l and a pH of 7.4.

[21] S. Derouiche, P. Mariot, M. Warnier, E. Vancauwenberghe, G. Bidaux, P. Gosset, B. Mauroy, J.-L. Bonnal, C. Slomianny, and P. Delcourt, Activation of TRPA1 channel by antibacterial agent triclosan induces VEGF secretion in human prostate cancer stromal cellstriclosan activates TRPA1 channel, Cancer Prev. Res. **10**, 177 (2017).

[22] O. P. Hamill, A. Marty, E. Neher, B. Sakmann, and F. J. Sigworth, Improved patch-clamp techniques for high-resolution current recording from cells and cell-free membrane patches, Pflugers Arch. - Eur. J. Physiol. **391**, 85 (1981).

[23] C. Faille, C. Jullien, F. Fontaine, M.-N. Bellon-Fontaine, C. Slomianny, and T. Benezech, Adhesion of *Bacillus* spores and *Escherichia coli* cells to inert surfaces: Role of surface hydrophobicity, Can. J. Microbiol. **48**, 728 (2002).